Research Article

Heat transfer enhancement on saturated porous samples using electrostatic precipitator process in *k-ε* turbulent model

Suwimon Saneewong Na Ayuttaya[*]

[*]*Department of Mechanical Engineering, Academic Division, Chulachomklao Royal Military Academy, Nakhon Nayok, Thailand 26001*

ATICLE INFO

ABSTRACT

An influence of the electrostatic precipitator process was numerically investigated for heat transfer enhancement on saturated porous samples in a *k-ε* turbulent model. The condition of the water entering a test section was the inlet temperature was 30 ℃ (303 K), and inlet velocity was tested in the range of 1 – 2.5 m/s. The electrical voltage and time varied between 0 – 30 kV and 0 – 1 s, respectively. The initial temperature of saturated porous samples was 10 ℃ (283 K), and both first and second samples were set in semicircle shapes. The numerical results within the water channel showed that the electric field and electric potential zone appeared and were concentrated when using the electrostatic precipitator process. The high electric voltage could increase disturbance and turbulence within the water channel. The maximum flow field zone appeared above the saturated porous sample area, and the maximum velocity field increased with the inlet velocity and electrical voltage. The maximum pressure was increased to the high voltages, but the pressure was marginally increased with high inlet velocity. The vorticity contour for an electrostatic precipitator process was more concentrated than without the electrostatic precipitator process. Therefore, the temperature contour line in case of high inlet velocity, electrical voltage, and time can be more disturbing than the other cases. In addition, heat from the water was transferred within the sample, so the temperature within the porous sample gradually increased. The fluid velocity within the front porous sample was more within the saturated porous samples than within the porous back sample. Therefore, the flow could move through and within the samples and induce temperature within both saturated porous samples. Finally, the heat transfer within samples was enhanced by fluid flow in the water channel, so the local heat transfer coefficient within samples was induced by the fluid velocity in the water channel.

© Published at www.ijtf.org

[*]*Corresponding e-mail*: joysuwimon1@hotmail.com (Suwimon Saneewong Na Ayuttaya)

1. Introduction

Sewage treatment technically removes substances that contaminate water, and after the waste treatment, water can be returned to the water cycle. For the hydrologic cycle, the water from treatment can be used in irrigation, agriculture, and various purposes [1]. Wastewater treatment plants may be distinguished by the type of wastewater to be treated. Numerous processes can be used to treat wastewater depending on the extent and type of the contamination. The treatment steps include physical, chemical, and biological treatment processes. The wastewater treatment process commonly screens for particle removal, settling, activated sludge, filtration, disinfection, and oxygen uptake. An activated sludge process is one type of wastewater treatment commonly employed using activated sludge bacteria [2 - 5]. This physical wastewater treatment process essentially involves the removal of large non-biodegradable and floating solids that frequently enter wastewater works. Most industrial wastewater treatment uses the physical wastewater treatment process to treat wastewater produced by industries as an undesirable by-product. The primary treatment is the evaporation of inorganic compounds. The method involves the heating of water with a solution. Process heat refers to the application of heat during industrial processes. In some processes, heat is used to manufacture many everyday products. With demanding to minimize energy consumption, alternative treatments are improved for thermal wastewater treatment. To improve sewage treatment, some researchers have paid great attention to developing thermal wastewater treatment by an electrostatic precipitator. It is a device for removing small particles from flowing water using electric force [6 - 8]. An electric heater is an electrical device that converts an electric current into heat and can enhance transport phenomena by lowering the energy supplied.

For the mechanism of the electrostatic precipitator process, a voltage of several thousand volts is applied between the wire electrode and plate ground. If the applied voltage is high enough, an electric corona discharge ionizes the air around the electrodes, which then ionizes the particles in the air stream. Due to the electrostatic force, the ionized particles are diverted toward the grounded plates. As a result, particles build upon the collection plates and are removed from the air stream. Two fluid types have been studied to improve the electrostatic precipitator performance, i.e., gas [9 - 16] and liquid [17 -20]. The motion of dust particles in electrostatic precipitation depends on the electric field, space charge, gas flow field, and characteristics of dust particles. The induced flow causes the total reaction to lean backward in the plane of rotation; it also reduces the perpendicular component of the total reaction and reduces the total rotor thrust. The first electrostatic precipitator process research was by Yamamoto and Velkoff [21]; they used experimental and theoretical studies of the secondary flow interaction in the electrostatic precipitator. The numerical results demonstrated close agreement with the experimental. Jerzy et al. [9] measured the flow field by the PIV method. The results showed that the PIV method investigates the field in ESP models. The secondary flow can increase the turbulence flow. This electrically generated turbulence is significant due to a strong interaction between the electric charge and the fluid flow. The secondary flows could impact the precipitation of small particles. Audrey et al. [12] investigated the synthesis of gas transformed from biomass gasification to ashes. Considering this issue, the feasibility of removing the particles was studied with an electrostatic precipitator at a high temperature (500 – 1000 °C), and pressure (0.1 – 1 MPa) was studied to develop a filtration process at as high a temperature feasible. It can describe the feasibility of an electrostatic precipitator to clean syngas at temperatures above 500 °C. Beelee et al. [19] investigated the liquid phase in airborne particles' precipitation functionality for a microfabricated electrostatic precipitator. The microfabricated electrostatic precipitator was placed into a flow control chamber with an aerosol particle from moving the gas streams. The corona current is measured during particle precipitation and can be visual observation. During a 60 s exposure of the oleic acid particles, the circuit resistivity was increased, and the electrode gap was decreased by approximately 50. In addition, the evolution of research in all electrostatic precipitator areas from the past until now is shown in Table 1.

Corresponding e-mail: joysuwimon1@hotmail.com (Suwimon Saneewong Na Ayuttaya)

Nomenclature

b	ion mobility, m^2/Vs	∇T	temperature gradient, K
C_p	specific heat capacity, J/K	V	electrical voltage, V
D	characteristic linear dimension, m	*Greek symbols*	
	electric flux density, C/m^2	ε	dielectric permittivity, F/m
	diffusion coefficient, cm^2/s	η	kinematics viscosity, m^2/s
E	electric field intensity, V/m	θ	angle of the inclined plate, ^{o}
f_E	electrophoretic force, C/m^2s	κ	permeability, m^2
h_L	local heat transfer coefficient, $W/m^2.K$	μ	viscosity, kg/ms
J	current density, A/m^2	*Subscripts*	
k	thermal conductivity, W/mK	b	back porous sample
n	unit normal vector	*eff*	effective
P	pressure, N/m^3	f	front porous sample
Q	flow rate, m^3/s	i	initial
q	space charge density, C/m^3	s	sample
t	Time, s	0	tip of electrode, initial
u	velocity, m/s	*Superscript*	
V	electrical voltage, V	T	matrix transpose

IJTST

Research Article

Table 1 (**Note:** *Lam* = Laminar flow, *Tur* = Turbulent flow, N/A = Not available)

Evolution of the electrostatic precipitator

References	Authors	Medium	Initial condition	Application	Methodology
[9]	Jerzy et al.	air	u_i = 0.2 m/s, V_0 = 24 kV	Particle precipitation process	Experiment
[10]	Lin and Kazimierz	air	Re_{lam}	Influence of the EHD flow	Simulation
[11]	Farnoosh et al.	air	Re_{tur}	Influence of the EHD flow	Simulation
[12]	Audrey et al.	ashes particles into air	T_i = 200 – 400ºC, P_i = 2-3 MPa	Biomass gasification	Experiment
[13]	Hao et al.	wet fuel gas	V_0 = 30 kV, T_i = 25ºC	control the emission SO_2	Experiment
[14]	Taghayi et al.	biofuel into air	u_i = 1.9 m/s, V_0 = 10 kV, T_i =150ºC, P_i = 25 Pa	Biomass gasification	Experiment
[15]	Deylami	SO_3 into air	N/A	The removal of sulfuric acid mist from flue gases	Experiment
[16]	Milad et al.	PM samples into air	Q_i = 75 LPM, V_0 = 12 kV	Toxicological studies	Experiment
[17]	Jingcai et al.	SO_3	V_0 = 15 - 35 kV	Control of sulfuric acid aerosol emission	Experiment
[18]	Liton and Chandra	soft nanoparticles into liquid	Q_i = 50 cm³/s, V_0 = 0 - 10 kV	Industry for removal of micron-sized particles from effluent gases.	Experiment
[19]	Beelee et al.	polydispersed liquid phase oleic acid particles	V_0 = 0 - 10 kV	Airborne liquid phase particles precipitation	Experiment
[20]	Islam et al.	aerosol is produced by vaporizing paraffin oil	Q_i = 0.53 g/min, V_0 = 8.1 – 16.8 kV	Device for control of particle emissions	Experiment+ Simulation

From a previous literature study, the main group of Electrohydrodynamics (*EHD*) applications was divided by Saneewong Na Ayuttaya [22]. The first group was the increased flow mechanism for *EHD* pumping and biomechanics application. The second group was the injection flow mechanism used in the droplet, electrospray, and microfluidics. The third group was the inducing flow mechanism used for electrostatic precipitator and *EHD* actuator application. The fourth group is the mixing process; it was used in boiling, heat and mass transfer, heat exchanger, and drying applications. For the third group (inducing flow mechanism), this mechanism of inducing flow requires a high Reynolds number (*Re*) and high electrical voltage removal of the particle into the medium. The experimental study presents most of the research because this machine is suitable for high *Re* or turbulent *Re,* so the numerical analysis is usually complex. In the different flow visualization, *Re* can predict flow patterns [23]. The low Re and high *Re* could be shown with laminar and turbulent flow, respectively. The turbulence flow appeared with differences in the fluid's speed and direction. There have been few research studies on the electrostatic precipitator process due to the complex interactions of the turbulent flow model under the electrostatic precipitator.

The flow visualization is necessary to show the control direction of particles because the flow

Corresponding e-mail: joysuwimon1@hotmail.com (Suwimon Saneewong Na Ayuttaya)

visualization in fluid dynamics is used to make the flow patterns visible to get qualitative or quantitative information on them [24, 25]. Nowadays, Computational fluid dynamics (*CFD*) can solve problems that involve flow visualization and fluid mechanics field; the fluid problems are numerically solved by *CFD* [26, 27]. In this study, the main electrostatic precipitator process involved the phenomena related to the direct conversion of electricity generation into kinetic energy, so heat transfer enhancement on saturated porous samples. This concept of the electrostatic precipitator process is a feasibility study based on the saturated porous samples improvement by heat transfer enhancement through the water channel. Furthermore, the flow visualization under the electrostatic precipitator process is conducted by numerical analysis, and all fields are systematically studied. The flow and temperature fields under the electrostatic precipitator process are numerically analyzed for heat transfer enhancement within the sample. Finally, the sample is the saturated porous medium, and the water channel is solved from the turbulent model ($k - \varepsilon$ model).

2. Numerical analyses

To study the interaction for heat transfer enhancement of saturated porous samples in a *k-ε* turbulent model under the electrostatic precipitator process, the main parts of the numerical analysis were obtained as follows:

2.1 Configuration

The water channel is created from three main parts, an electric field, fluid flow, and the temperature field. The dimension of water channel is X = 15 cm (long) × Y = 2.5 cm (high) and the physical model geometry is shown in Fig. 1. The Y-axis is defined for the channel flow. In fluid mechanics and hydraulics, channel flow is an internal flow in which the confining walls change the hydrodynamic structure of the flow from an arbitrary state at the channel inlet to a certain state at the outlet [28]. From assumption, clays are removed from the water tube for wastewater treatment. Clays are assumed to be saturated porous samples composed of soil and water. The two saturated porous samples are

semicircle-shaped; the radius is 1 cm, and they are stuck to the bottom wall of the water channel. The center of the first and second semicircle shapes (saturated porous sample) are fixed at (4, 0) and (8, 0), respectively. The first semicircle shape (front porous sample; T_f) and second semicircle shape (back porous sample; T_b) appear at the front and behind the water channel, respectively. The conjugate method investigates the interface zone between water and sample. Within the water channel, the diameter of the circle electrode (*E*) is 0.01 cm, and plate ground (*G*) is 1 cm (long) × 0.1 cm (high). Three-circle electrodes and the one plate ground are suspended in each sample above the saturated porous sample. From a previous study, the electric field can drive from electrode to ground and is dense between electrode and ground zone [29], so a plate ground is installed behind the circle ground when the flow direction moves from left to right. In this setup of the water entering a test section, the uniform initial temperature in the water channel (T_i) is 30 ℃, and the initial temperature of the saturated porous sample (T_s) is 10 ℃. The electrical voltage (V_0) is varied from 0 to 30 kV, it is incremented by 5 kV; the inlet velocity of water (u_i) is tested in the range of 1 – 2.5 m/s, it is incremented by 0.5 m/s; and the time varies in a range 0 – 1 s, it is incremented by 0.05 s. From Equation 4, the Reynolds number (Re) is composed of characteristic linear dimension (high of water channel), density and viscosity of water and inlet water flow (u_i = 1 - 2.5 m/s). The laminar flow occurs when Re$_D$ < 2300, and turbulent flow occurs when Re$_D$ > 2900 [29]. When u_i = 1 - 2.5 m/s, the rage of Re is 31,172 – 77,930, and Re can be considered in a turbulent flow. It can be seen that the turbulent model ($k - \varepsilon$ model) is solved in the water channel. In the simulation, heat transfer of saturated porous samples is enhanced under an electrostatic precipitator. A domain subdivision is used for the simulation, which is made up of the inside water channel, where the electric force, fluid motion, and heat transfer enhancement equations are systematically solved in the *k-ε* turbulent model. The classical properties of water flow are shown in Table 2 [30, 31], and the thermal properties of water flow, water (liquid; *l*), and clay (solid, *s*)

are shown in Table 3 [30, 31]. The saturated porous sample consists of clay with only water in the voids.

2.2 Equations

The numerical modeling based on the concept of an electrostatic precipitator process has been developed for the heat transfer enhancement within saturated porous samples in the *k-ε* turbulent model. Within the water channel, the fluid physical properties are constant and incompressible fluid. Concerning the velocity, a channel profile is imposed at the inlet with a turbulent intensity. The continuity equation (Eq. (1)) and Navier–Stokes equation coupled with the Coulomb force equation (Eq. (2)) are expressed as:

$$\nabla \cdot \vec{u} = 0 , \tag{1}$$

$$\rho \left[\frac{\partial \vec{u}}{\partial t} + (\vec{u} \cdot \nabla) \vec{u} \right] = -\nabla \bar{P} + (\mu + \mu_{tur}) \nabla^2 \vec{u} + \vec{f}_E , \tag{2}$$

where u is water flow velocity, t is time, P is pressure, ρ is the density of water and μ viscosity of water. Where μ_{tur} is the viscosity of water in a turbulent flow $\mu_{tur} / \rho = C_\mu k^2 / \varepsilon$.

The vortex structures or vorticity (ω) using an electrostatic precipitator is described by Saneewong Na Ayuttaya et al. [32]. When high electrical voltage is exposed to fluid flow, the fluid flow is created by ions generated in the corona discharge near the sharp electrode drifting to the ground. As a result, the momentum of fluid flow is enhanced, and the primary flow is generated. The primary flow, ionized air, moves from electrode to ground to induce the shear flow or secondary flow, so-called vorticity. Shear flow then appeared due to the difference in fluid velocity between the charged and uncharged fluid flow.

The strength of the vortex structure subjected to an electric field is assessed through vorticity (ω), as shown in Eq. (3).

$$\vec{\omega} = \nabla \times \vec{u} , \tag{3}$$

The Reynolds number (*Re*) is an important dimensionless quantity in fluid mechanics used to predict flow patterns in different fluid flow situations, as shown in Eq. (4) below.

$$Re = \frac{\rho \vec{u} D}{\mu} , \tag{4}$$

The electric force (f_E) relating to fluid flow can be expressed in

$$\vec{f}_E = q\vec{E} , \tag{5}$$

where E is electric field and space charge density (q) is calculated by Griffiths [33]. In this idea, the electric charge is treated as a continuum of charge distributed over a region of the area. The dielectric properties are homogeneity, and the electric field line is driven from the electrode and induced to the ground. The electric field is calculated by using Maxwell's equations (Eqs. (6), (7), (8) and (9)) shown below:

$$\nabla \cdot \varepsilon \vec{E} = q , \tag{6}$$

$$\vec{E} = -\nabla V , \tag{7}$$

$$\nabla \cdot J + \frac{\partial q}{\partial t} = 0 , \tag{8}$$

$$J = q\vec{u} + (\vec{u} \cdot \nabla)(\varepsilon \vec{E}) - b\nabla q , \tag{9}$$

where ε is dielectric permittivity, V is electrical voltage, J is current density, and b is ion mobility.

With heat transfer under the electrostatic precipitator process, the temperature in the water

Table 2
Classical properties

Modeling parameter	$b\,(\text{m}^2/\text{V.s})$	$\varepsilon\,(\text{F/m})$	ϕ	$\kappa\,(\text{m}^2)$	saturation	Ref
water	1.80×10^{-4}	8.85×10^{-12}	-	-	1	[30]
solid	-	-	0.55	5.00×10^{-17}	-	[31]

Modeling parameter	$\rho\,(\text{kg/m}^3)$	$\mu\,(\text{kg/ms})$	$k\,(\text{W/mK})$	$C_p\,(\text{kJ/kgK})$	Ref
water in channel	996	0.799×10^{-3}	0.570	4.117	[30]
water in porous	999	1.30×10^{-3}	0.582	4.192	[30]
solid in porous	1500	-	2.000	0.878	[31]

channel is higher than in the saturated porous sample, so the heat transfer has appeared. This idea can be used as implementation guidance for removing dry clay in the water tube under the electrostatic precipitator process. The validity of the following statements, the effect of buoyancy is negligible, and the thermal property using supercritical fluid is constant. The isotropic and homogeneous are used for the saturated porous medium, and the temperature distribution of the water is calculated from the energy equations. The governing equations describing the heat transfer enhancement within the channel flow and the saturated porous medium are calculated from Eqs. (10) and (11), respectively.

$$\rho C_p \left[\frac{\partial T}{\partial t} + \vec{u}\nabla T \right] = k\left(\nabla^2 T\right), \tag{10}$$

$$\frac{\partial T}{\partial t} = \frac{k_{eff}}{\left(\rho_s C_p\right)_{eff}} \nabla^2 T , \tag{11}$$

where T is temperature, k thermal conductivity, and C_p the specific heat capacity. The effective thermal conductivity (k_{eff}) in a porous medium is calculated by $k_{eff} = (1-\phi)\kappa_s + \phi\kappa_l$ [34] (where κ is permeability, ϕ is porosity, and subscript s and l are clay (solid, s) and water (liquid; l) phase). To investigate the local heat transfer coefficient (h_L) (Eq.(12)) within the saturated porous sample surface, the porous medium material is stuck to the bottom of the water channel, and the upper surface is exposed to hot water flow. So local convective heat transfer is defined by the thermal equilibrium equation:

$$h_L = -\frac{k}{\Delta T}\frac{\partial T}{\partial n} \tag{12}.$$

2.3 Boundary condition

The boundary condition of the water channel and saturated porous sample under the electrostatic precipitator process is shown in Fig. 2. For symbol, the normal font for solving an electric field, all of the outer boundary conditions of an electric field are defined with zero charge symmetry ($n \cdot D = 0$). The boundary conditions of electrode and ground are $V = V_0$ and $V = 0$, respectively. In the bold font for solving the flow field, the inlet velocity boundary

condition $\vec{u} = \vec{u}_i$ and pressure of outlet boundary condition are considered with zero viscous stress ($\eta(\nabla\vec{u} + (\nabla\vec{u})^T \cdot n = 0$). This boundary condition specifies vanishing viscous stress along with a Dirichlet condition on the pressure ($\vec{P} = \vec{P}_0$). No-slip boundary conditions are computed for the upper and lower channel flow ($\vec{u} = 0$). In the oblique font for solving the temperature field, the uniform initial temperature of the water channel is defined as $T = T_i$. The other surface is considered an insulated boundary condition ($-n \cdot (-k\nabla T) = 0$). The interface area between the sample and water in the channel is exposed to water flow. The conjugate method can solve the interface between heat and fluid flow; the interface is solved by $-n_u \cdot (-k_u\nabla T_u + \rho_u c_{p,u}\vec{u}_u T_u) - n_d \cdot (-k_d\nabla T_d + \rho_d c_{p,d}\vec{u}_d T_d) = 0$.

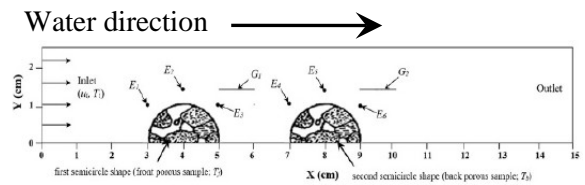where u and d are the symbol of the upper and the lower interfaces.

Fig. 1 Physical model geometry

2.4 Finite element method

Considering that this research investigates heat transfer within samples in water channels using an electrostatic precipitator. Calculations must be performed for the saturated porous medium, and the water channel is solved from the $k - \varepsilon$ turbulent model. Therefore, computational fluid dynamics (*CFD*) using the finite element method (FEM) is conducted to investigate flow and temperature fields under the electrostatic precipitator process. The simulation and conditions are involved for all parameters, with a point of improving the device's design to electrostatic precipitator process for removing contaminants from water tube. This research involves a complex problem that combines electrostatic and fluid mechanics and heat transfer enhancement in the water channel. This work
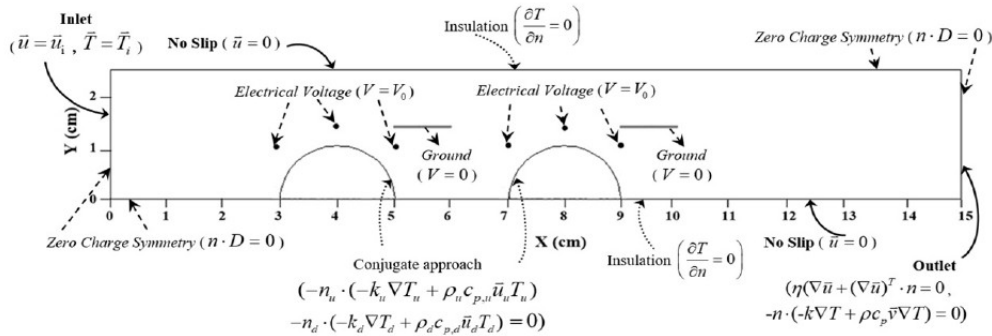
Fig. 2 boundary condition of the water channel and the saturated porous sample
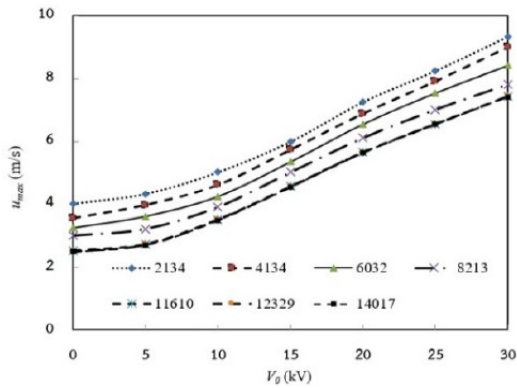

Fig. 3. Relationship between maximum velocity and electrical voltage from the simulation with the different number of meshes

involves a complex problem that combines electrostatics with fluid mechanics and heat transfer enhancement in the water channel. The electric field is the main parameter for the generation of corona wind. For this purpose, the commercial software (Finite Element Method Electromagnetics) [35, 36] is used to assess the various parameters; as a result, the optimal design is selected. In this idea, a finite-dimensional space of some solutions, a number of points in the boundary, and the collocation points are used for the given equation. The water channel flow model is discretized using a triangular element. The Lagrange quadratic approximates each parameter's electric field, flow field, and temperature distribution variation. The convergence test of the electrical voltage of 30 kV is carried out to identify the suitable numbers of elements required and the relationship between temperature and time from simulations at the interface between

the water channel and sample for different meshes. The convergence curve resulting from the convergence test and the relationship between maximum velocity and electrical voltage from the simulation with the different number of meshes is shown in Fig. 3. The system of governing equations is solved with the unsymmetrical multi-frontal method. The number of elements independent of element density was 11,610, and a dimensionless time step of 1×10^{-4} to ensure numerical stability and accuracy. Therefore, it can be assumed that the accuracy of the numerical results is independent of the number of elements.

3. Results and discussion

The saturated porous sample improvement through the water channel is systematically proposed. The k-ε turbulent model is combined with the electrostatic, flow field, and temperature model. This feasibility study is based on the concept of the electrostatic precipitator process. Where the electrical voltage (V_0) is tested from 0 to 30 kV, it is incremented by 5 kV; the inlet velocity of water (u_i) is tested in the range of 1 – 2.5 m/s, it is incremented by 0.5 m/s; and time vary in a range 0 – 1 s, it is incremented by 0.05 s. The uniform initial temperature of water (T_i) is 30 ºC (303 K), and the initial temperature of saturated porous samples (T_s) is 10 ºC (283 K).

The first part shows the verification of the model for numerical flow visualization. Then, water flow transport within the k-ε turbulent model was compared to the electric field, flow field, pressure field, vorticity field, and temperature field with and without the electrostatic precipitator process. Finally, the saturated porous

samples' flow and temperature fields were compared to the first semicircle shape (front porous sample; T_f) and the second semicircle shape (back porous sample; T_b).

3.1 Verification of the mode

Figure 4 shows the experimental and numerical setup to verify the accuracy of computational fluid dynamics (CFD) by using FEM to investigate the electric and flow fields. The numerical result is validated with the experimental result. The flow visualization from the experimental setup is generated using the oil smoke to produce a clear image of flow visualization, as shown in Fig. 4 (a). The wind tunnel is mostly made of acrylic plates. The dimension of tunnel is 1.5 m (long) × 0.3 m (high) × 0.3 m (wide). The jet airflow is supplied from a blower (u_i = 1 m/s) and is controlled by the flow meter. The acrylic inclined plate's (the dimension of the inclined plate is fixed at 15 × 15 cm^2) angle (θ) is varied from 0 to 90°, by 30° increments. The spotlight LED 500 W is installed at the outlet of the rectangular duct, and the light direction is averse to the flow direction. The high voltage power supply creates a high electrical voltage (V_0). The boundary condition for numerical modeling has been formulated to predict the electric field and flow field within the rectangular duct, as shown in Fig. 4 (b). The present simulated result is solved by the finite element method using the collocation method. From classical properties, ion mobility (b) is 1.8×10^{-4} m^2/Vs, dielectric permittivity (ε) is 8.85×10^{-12} F/m, density (ρ) is 1.2 kg/m^3 and kinematics viscosity (η) is 1.56×10^{-5} m^2/s. The experimental result by oil smoke technique and the simulated result by cell Reynolds number are shown in the airflow motion. The cell Reynolds number characteristics or particle trajectories can be taught as the Peclet number. The cell Reynolds number characteristics or particle trajectories can describe the Peclet number. The Reynolds Number is the ratio of inertial force divided by viscous forces, while the Peclet number is the ratio of convective heat transfer divided by diffusive fluxes [37]. In all cases, the air has flowed in the cross-flow direction (left to right), avoids the inclined plate, and is the obstacle. The flow separation has appeared behind the inclined plate due to

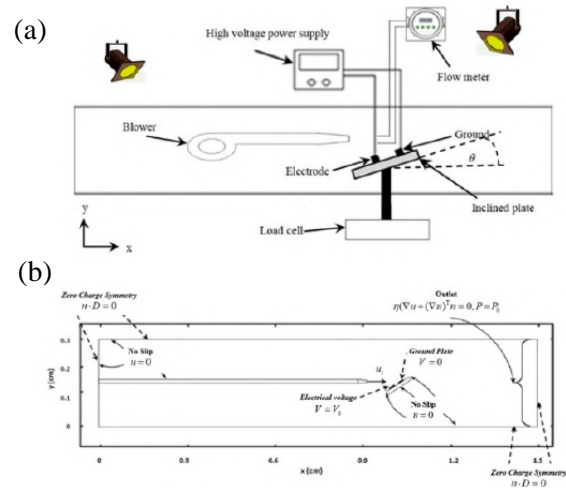the weak adverse pressure gradients, and the momentum of upstream forces is weakening.

**Fig. 4.** Verification of the model (a) experimental setup (b) boundary condition for numerical modeling

In case absent electrostatic precipitator process (Fig. 5), the angle of the inclined plate (θ) is varied to show the flow visualization from the experimental (Fig. 5 (a - c)) and numerical setup Fig. 5 (d - f)). To present the simulated result, the flow visualization is shown both streamline and surface boundaries. For (θ = 15° (Fig. 5 (a)), the airflow is moved through the inclined plate, and airflow is not turbulent, but the airflow is turbulent with the inclined plate at a 45° angle of attack (Fig. 5 (b)). The airflow is strongly turbulent in the case of the high angle of the inclined plate, as shown in Fig. 5 (c). The flow visualization by oil smoke technique (Fig. 5 (a - c)) is a similar trend to simulation results (Fig. 5 (d - f)). The flow visualization in case of θ= 15° (Fig. 5 (a)), θ= 45° (Fig. 5 (b)) and θ= 75° (Fig. 5 (c)) are similar trend in case of θ= 15° (Fig. 5 (d)), θ = 45° (Fig. 5 (e)) and θ = 75° (Fig. 5 (f)), respectively.

With the electrostatic precipitator process (Fig. 6), the flow visualization of the experimental setup (Fig. 6 (a-c)) is compared with the simulated result (Fig. 6 (d - f)). The electrical voltage and the jet airflow are fixed at V_0 = 10 kV. The airflow in case of θ = 45° (Fig. 6 (b)) is more turbulent than in case of θ = 15° (Fig. 6 (a)). In the case of the high angle of the inclined plate (θ = 75° (Fig. 6 (c)), the airflow is extremely turbulent. The flow visualization in case of θ =

15º (Fig. 6 (a)), $\theta = 45$º (Fig. 6 (b)) and $\theta = 75$º (Fig. 6 (c)) are similar trend with in case of $\theta = 15$º (Fig. 6 (d)), $\theta = 45$º (Fig. 6 (e)) and $\theta = 75$º (Fig. 6 (f)), respectively. It can be seen that a similar trend of the airflow distribution has appeared in both cases.
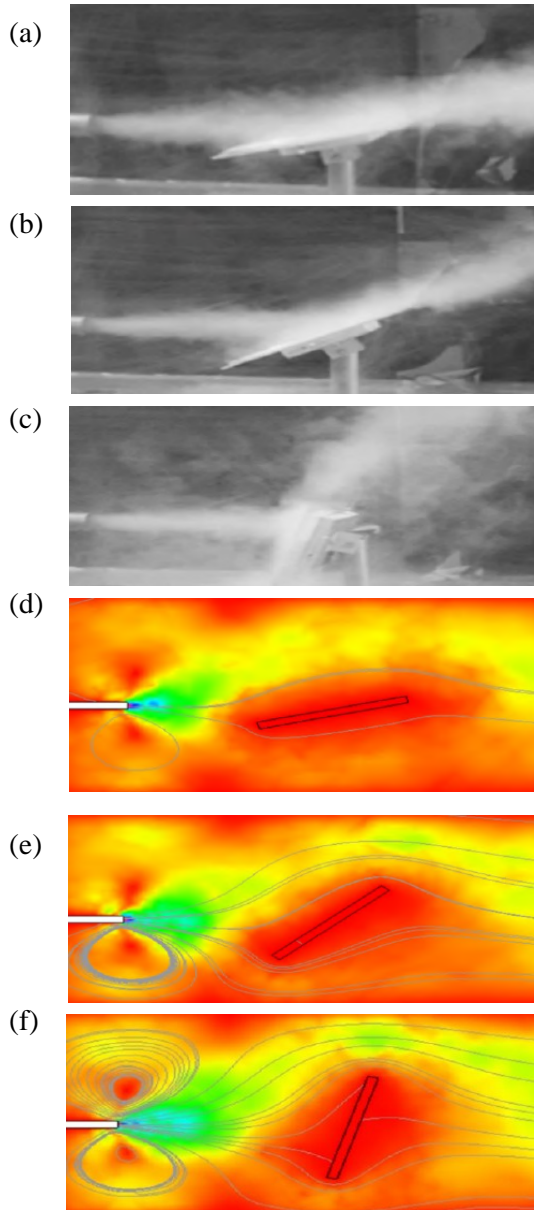

Fig. 5. Comparison of flow visualization between experimental and simulated result in absent electrostatic precipitator process and $u_i = 1.0$ m/s in the various angles of an inclined plate (a) $\theta = 15$º, experimental result (b) $\theta = 45$º, experimental result (c) $\theta = 75$º, experimental result (d) $\theta = 15$º, simulated result (e) $\theta = 45$º, simulated result (f) $\theta = 75$º, simulated result
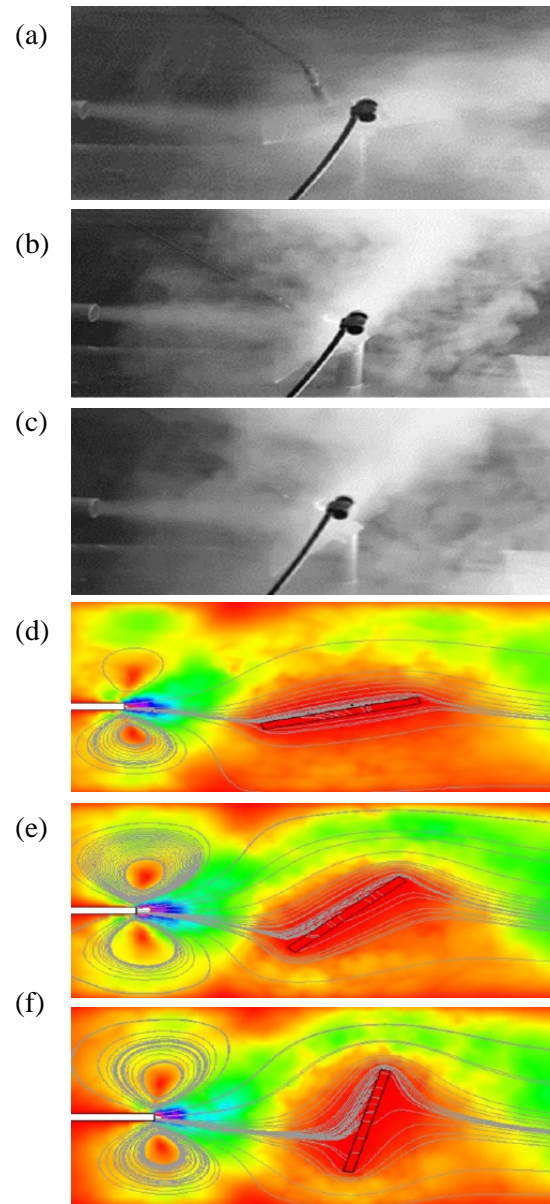
Fig. 6. Comparison of flow visualization between experimental and simulated result under electrostatic precipitator process ($V_0 = 10$ kV) and $u_i = 1.0$ m/s in the various angles of an inclined plate (a) $\theta = 15$º, experimental result (b) $\theta = 45$º, experimental result (c) $\theta = 75$º, experimental result (d) $\theta = 15$º, simulated result (e) $\theta = 45$º, simulated result (f) $\theta = 75$º, simulated result

3.2 Effect of electric field distribution

An electric field is a physical field composed of electrically charged particles and can affect all other charged particles in the field. The electric field within the water channel under the k-ε turbulent model is shown in Fig. 7.
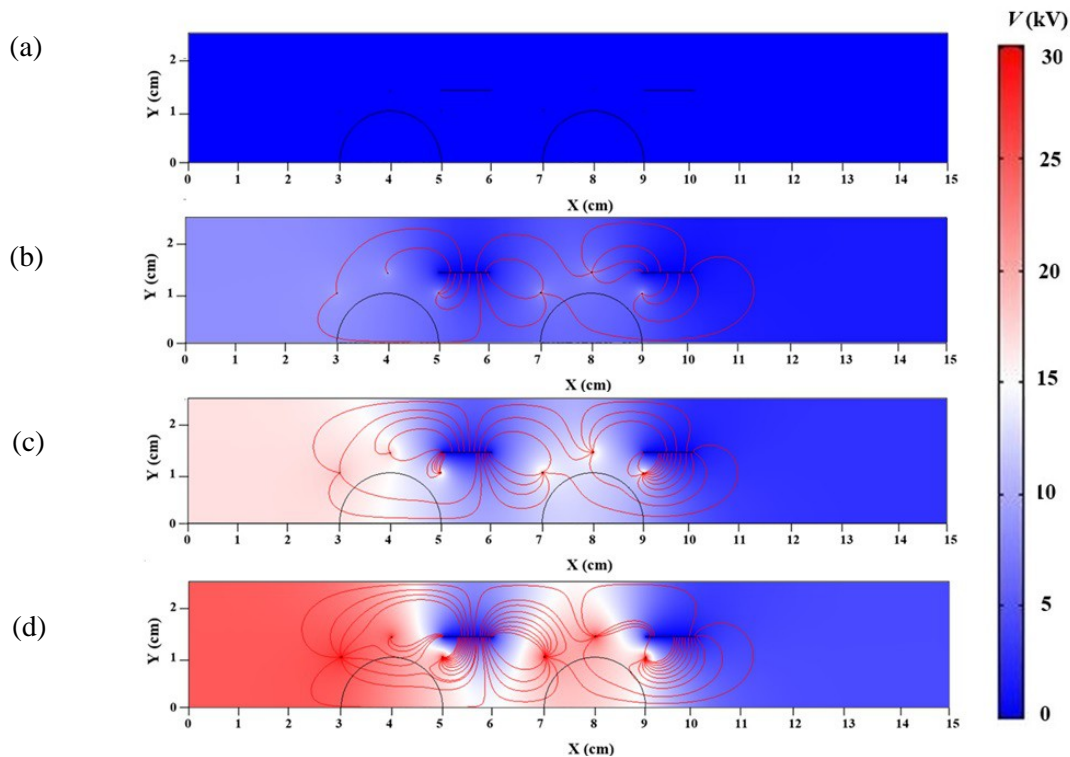
Fig. 7 Electric field within water channel (a) $V_0 = 0$ kV (b) $V_0 = 10$ kV (c) $V_0 = 20$ kV (d) $V_0 = 30$ kV with electric field lines and electric potential zone
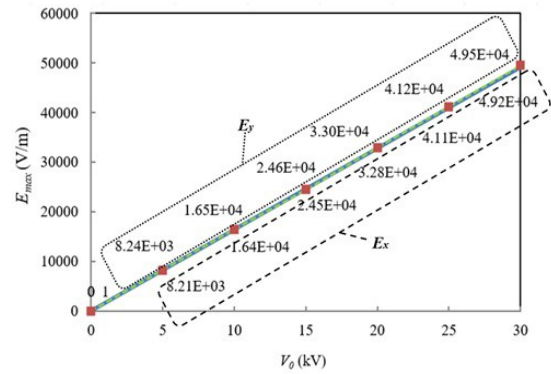
In the case of the absent electrostatic precipitator process (Fig. 7 (a)), the electric field and the electric potential zone have not appeared. Instead, the electric field and potential zone appear and are concentrated in the case of using the electrostatic precipitator process. The electric field moves outward from the tip of circle electrodes ($E_1, E_2, E_3, E_4, E_5, E_6$) to plate grounds ($G_1, G_2$), and the electric field lines are turbulent at both of electrode and ground zone [32]. The electric potential zone is more expanded and more turbulent with increasing the electrical voltage, as shown in Fig. 7 (b) – 7 (d)). In addition, the semicircle shapes are considered for a feasibility study on the development of saturated porous samples improvement. The circle electrodes (E_1, E_2, E_3) and plate ground (G_1) is set up for the first semicircle shape (front porous sample; T_f), and the circle electrodes (E_3, E_4, E_6) and the plate ground (G_2) is set up for the second semicircle shape (back porous sample; T_b). From Fig., some electric field lines of E_4 and E_5 are moved to G_1 and G_2. Typically, the electric

field lines are moved to the shortest distance, but the strength of electrical voltage can disturb, so the electric fields are moved to both grounds. According to the above data, the disturbance of electric field distribution can concentrate more electric potential, resulting in a turbulent area appearing. Fig. 8 shows the value of an electric field at the line of the cross-section of the X-axis through the middle of the water channel. It can be seen that the first position or edge of the ground is accumulated the high electric force, so the maximum value of the electric field appears. The electric field zone is influenced around the electrode and ground zone above the saturated porous sample area. Therefore, the value of an electric field is increased with the electrical voltage increasing. Furthermore, the maximum value of X - electric field (E_x) and Y - electric field (E_y) are increased with the electrical voltage increasing, as shown in Fig. 9. A graph of the maximum value of X- electric field (E_x) is related to Y - electric field (E_y). The maximum value of X - electric field (E_x) and Y- electric field
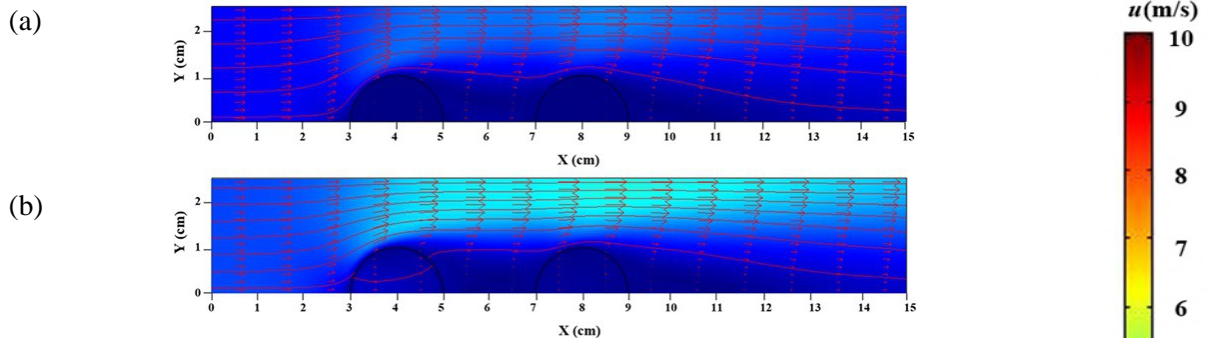
(E_y) show a variable straight line indicating the electrical voltage ($E_{max} \propto E_x \propto E_y \propto V_0$).
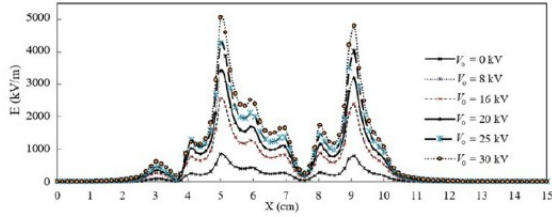

Fig. 8 Value of an electric field at cross sections line of the X-axis through the middle of the water channel ($X_i, Y_i = 0, 0.0125$ and $X_j, Y_j = 0.15, 0.0125$)


Fig. 9 Maximum value of electric field (E_{max}) in various electrical voltage consider both of X- electric field (E_x) and Y- electric field (E_y)

Fig. 10 Flow field within water channel and absent electrostatic precipitator process (a) $u_i = 1.0$ m/s (b) $u_i = 2.0$ m/s with streamline and arrow plot
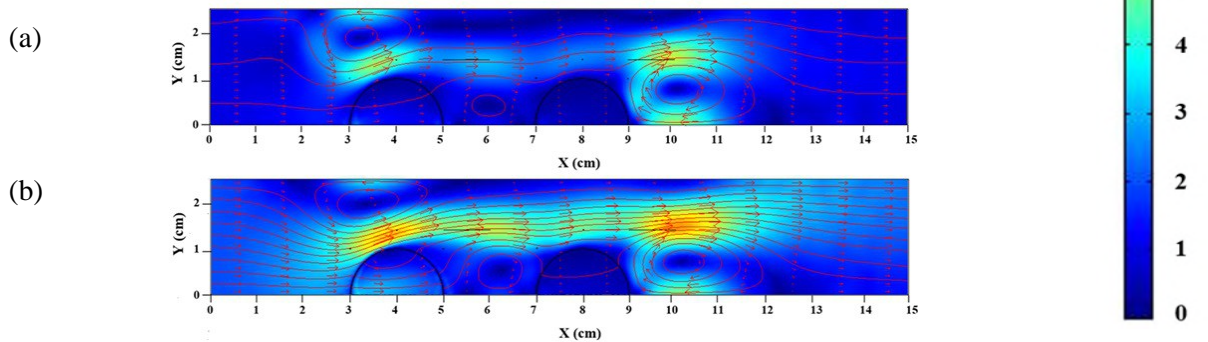
Fig. 11 Flow field within the water channel under electrostatic precipitator process and $V_0 = 20$ kV (a) $u_i = 1.0$ m/s (b) $u_i = 2.0$ m/s with streamline and arrow plot
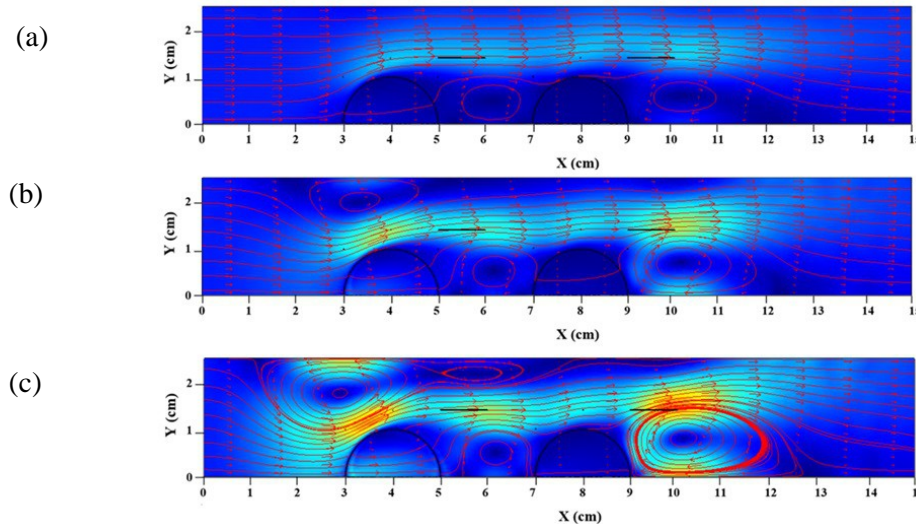
Fig. 12 Flow field within water channel under electrostatic precipitator process and $u_i = 1.5$ m/s (a) $V_0 = 10$ kV (b) $V_0 = 20$ kV (c) $V_0 = 30$ kV with streamline and arrow plot

3.3 Effect of flow field distribution

The eulerian specification specifies the flow field, and fluid motion is focused on the time the fluid move pass. the flow visualization is observed with the fluid passing the fixed location; visualized by observing the test section and watching the fluid pass the fixed location. In this study, the flow field in fluid mechanics is a space or region with a distribution of physical quantity. This water flow quantity exists at each point in this physical space. In the absent electrostatic precipitator process, the flow field within the water channel under the k-ε turbulent model is shown in Fig. 10. The flow field is moving from the left to the right and avoiding both saturated porous samples (first semicircle shape (front porous sample; T_f) and second semicircle shape (back porous sample; T_b)). The maximum flow field zone has appeared above the saturated porous sample area, and the maximum velocity field increases with inlet velocity. In the case of high inlet velocity (Fig. 10 (b)), the maximum velocity zone is higher than in cast of low inlet velocity (Fig. 10 (a)).

The flow field using the electrostatic precipitator process ($V_0 = 20$ kV) is shown in Fig. 11. The three cells of circulating fluids have appeared within the water channel under the k-ε turbulent model. The big cell circulated counterclockwise for the first cell, appearing above the first semicircle shape (front porous sample) zone. For the second cell, the small cell circulated clockwise, and it appears between the saturated porous samples (first semicircle shape (front porous sample) and second semicircle shape (back porous sample)). The big cell circulated in the clockwise direction for the third cell, appearing above the second semicircle shape (back porous sample) zone. In addition, the main effect of the first and the third cells is the shear flow effect. The shear flow is influenced by differences in velocities for the fluid caused by fluid charging effects [36]. The charged fluid flow from primary flow leads to secondary flow. The electric force is influenced by the first and the third cells, but the initial force from the pore between the first and second semicircle shape is influenced by the second cell. The three cells in case of high inlet velocity ($u_i = 2.0$ m/s) (Fig. 11 (b)) are stronger and more expanded than the three cells in case of low inlet velocity ($u_i = 1.0$ m/s) (Fig. 11 (a)).

As the electrostatic precipitator process increases (electrical voltage increases), inlet velocity is fixed at $u_i = 1.5$ m/s, as shown in Fig. 12. The maximum flow has appeared around the electrode and ground zone. Fig. 12 (a)) shows the low electrical voltage ($V_0 = 10$ kV); the two cells have appeared within the water channel under the k-ε turbulent model. The two cells are circulated clockwise; the first and the second cells appear between the first and the second semicircle shapes and behind the second semicircle shape, respectively. Fig. 12 (b)) shows the medium electrical voltage ($V_0 = 20$ kV); the three cells have appeared within the water channel under the k-ε turbulent model. The first cell circulated counterclockwise and appeared above the first semicircle shape zone. The second and the third cells are circulated clockwise, and they have appeared behind both of the second semicircle shapes. In the case of high electrical voltage ($V_0 = 30$ kV), the four cells are circulated, as shown in Fig. 12 (c). The first big cell is circulated counterclockwise, appearing above the first semicircle shape zone. The second cell is circulated in the clockwise direction, and it has appeared between the first and the second semicircle shapes. The third biggest cell is circulated in the clockwise direction, appearing behind the back semicircle shape zone. From the above data, the main effect of the first and third cells in the shear flow and the main effect of the second cell is the initial force. As a result, the small fourth cell is circulated on the top of the water channel under the k-ε turbulence model, which is influenced by the initial force of the first cell. It can be seen that the increasing electrical voltage influences the strength of the electric force. The high electric voltage can increase disturbance and turbulence within the water channel. The above result showed that electric force is induced by the electric field (Fig. 7), resulting in the circulating flow that can induce fluid flow (Fig. 11, 12) within the water channel under the k-ε turbulence model. Increasing electric field (Fig. 12 (c)) causes the strength of flow field distribution (Fig. 7 (d)).

Fig. 13 and 14 show the relation between inlet velocity and electrical voltage. The inlet velocity of water (u_i) is tested in the range of 1

– 2.5 m/s, it is incremented by 0.5 m/s, and the electrical voltage (V_0) is varied from 0 to 30 kV, is incremented by 5 kV. The maximum velocity (u_{max}) in various inlet velocities and electrical voltage is considered in Fig. 13 (a). The maximum velocity is increased with inlet velocity and electrical voltage increasing. The maximum velocity ratio (($u_R = u_{max}/u_i$) is shown in Fig. 13 (b); it can be seen that in the case of inlet velocity is high, the maximum velocity ratio is higher than that case of inlet velocity is low. The maximum velocity ratio in the case of high electrical voltage is lower than in the case of low electrical voltage. The maximum velocity (u_{max}) and maximum velocity ratio (u_R) are related to inlet velocity. The maximum velocity (u_{max}) graphs show a variable straight line indicating the inlet velocity increasing. In other words, the maximum velocity ratio (u_R) is inversely proportional to inlet velocity increasing. The correlation of data is $u_{max} \propto u_i \propto 1/u_R$).
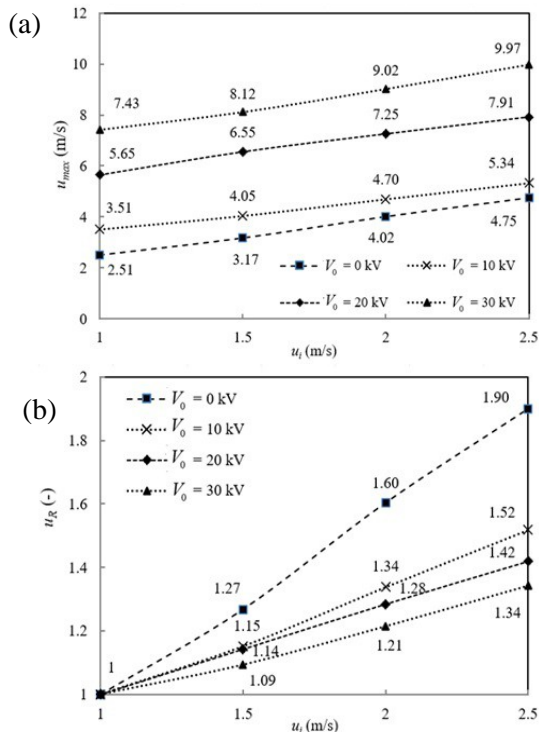
(a)

(b)

Fig. 13 Comparison between inlet velocity in various electrical voltage in case of (a) maximum velocity (b) maximum velocity ratio

Fig. 14 (a) shows that the maximum velocity (u_{max}) is increased with electrical voltage and inlet velocity increasing. The maximum velocity ratio (u_R) increases with the electrical

voltage but decreases with inlet velocity increases, as shown in Fig. 14 (b). The graphs of maximum velocity (u_{max}) and the maximum velocity ratio (u_R) are variable exponential lines for the electrical voltage (V_0), $u_{max} \propto u_R \propto V_0^2$. The maximum velocity ratio in case of $V_0 = 0$ kV and $u_i = 2.5$ m/s (Fig. 13 (b)) and $V_0 = 30$ kV and $u_i = 1.0$ m/s (Fig. 14 (b)) are about 1.90 and 2.96 times, respectively. The maximum velocity ratio in case of $V_0 = 30$ kV and $u_i = 1.0$ m/s is higher than in case of $V_0 = 0$ kV and $u_i = 2.5$ m/s. As can be seen that electric force is superior to inertial force.
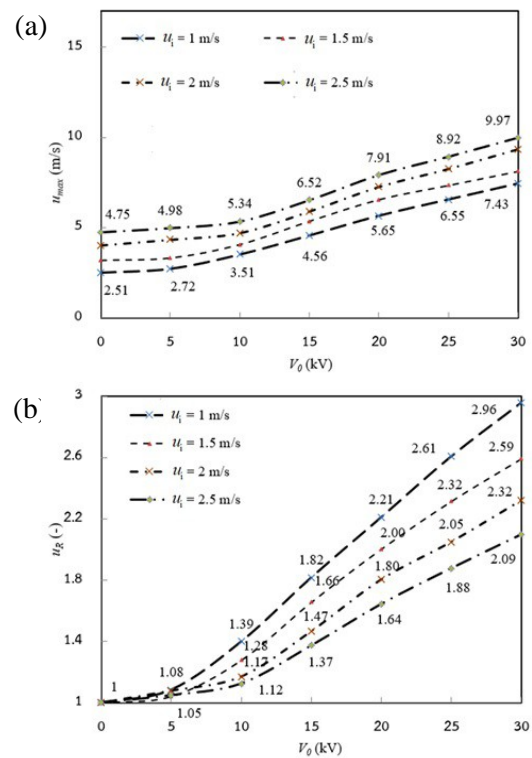
(a)

(b)

Fig. 14 Comparison between electrical voltage in various inlet velocity in case of (a) maximum velocity (b) maximum velocity ratio

3.4 Effect of pressure field distribution

The pressure field within the water channel with and without the electrostatic precipitator process is compared in Fig. 15. The pressure field is a general field component, represented in the Lagrangian and Hamiltonian of an arbitrary physical system, including the term with the energy of particles in the pressure field and the term with field energy. The upstream pressure is generally greater than the downstream pressure. The

pressure field within the water channel under the k-ε turbulent model is not concentrated in case of an absent electrostatic precipitator process (Fig. 15 (a - b)). The contour lines are swirl around the porous samples and the pressure field in case of low inlet velocity ($u_i = 1.5$ m/s) (Fig. 15 (a)) and high inlet velocity ($u_i = 2.5$ m/s) (Fig. 15 (b)) are gradually constant in both cases. In case of electrostatic precipitator process ($V_0 = 15$ kV (Fig. 15 (c - d)), the contour lines are move above porous samples and the upstream pressure field in case of low inlet velocity ($u_i = 1.5$ m/s) (Fig. 15 (c)) and high inlet velocity ($u_i = 2.5$ m/s) (Fig. 15 (d)) are greater than the downstream pressure. The pressure field with the electrostatic precipitator process is more concentrated than

without. It can be seen that the electrostatic precipitator process is more influenced than the inlet velocity within the water channel under the k-ε turbulent model. The maximum pressure (P_{max}) in various inlet velocities (u_i) and electrical voltage (V_0) is shown in Fig. 16. For Fig. 16 (a), the maximum pressure is increased with the electrical voltage increasing, but it is little increased with inlet velocity increasing. On the other hand, the maximum pressure increased as the voltage increased, and it is a little different with various inlet velocities, as shown in Fig 16 (b). However, higher inlet velocity and high electrical voltage can induce more pressure than in other cases. The graph of maximum pressure (P_{max}) is the variable exponential line for the electrical voltage (V_0), $P_{max} \propto V_0^2$.
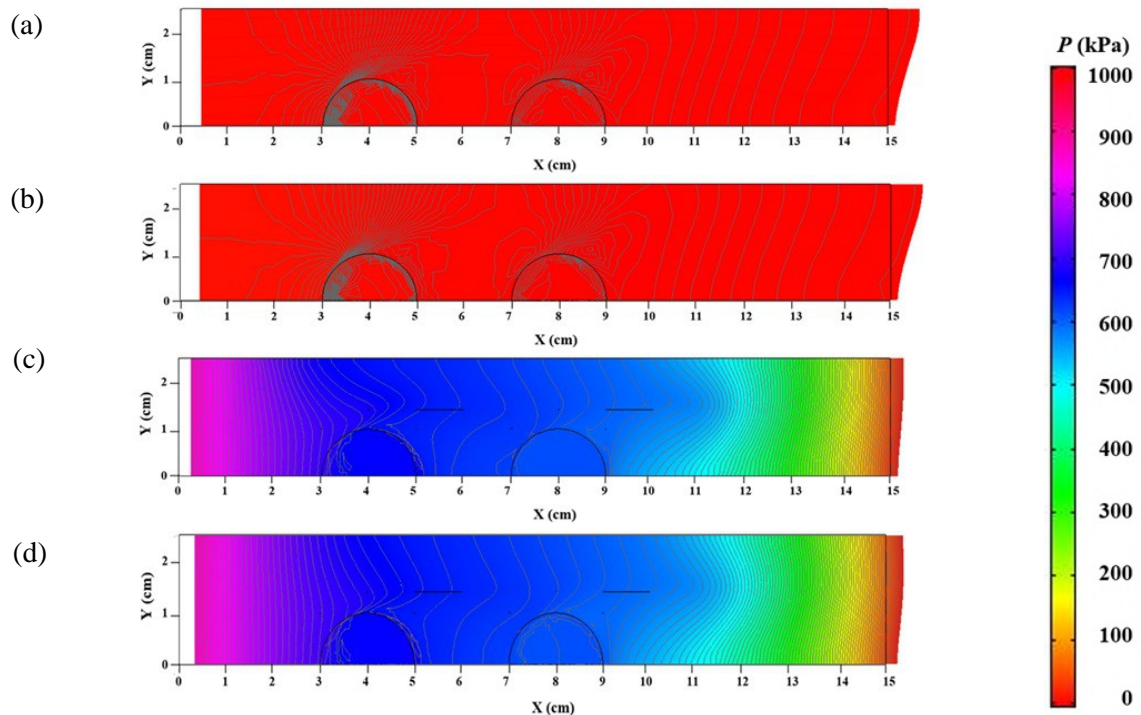

Fig. 15 Pressure field within water channel (a) $V_0 = 0$ kV and $u_i = 1.5$ m/s (b) $V_0 = 0$ kV and $u_i = 2.5$ m/s (c) $V_0 = 15$ kV and $u_i = 1.5$ m/s (d) $V_0 = 15$ kV and $u_i = 2.5$ m/s with contour plot and deformed shape
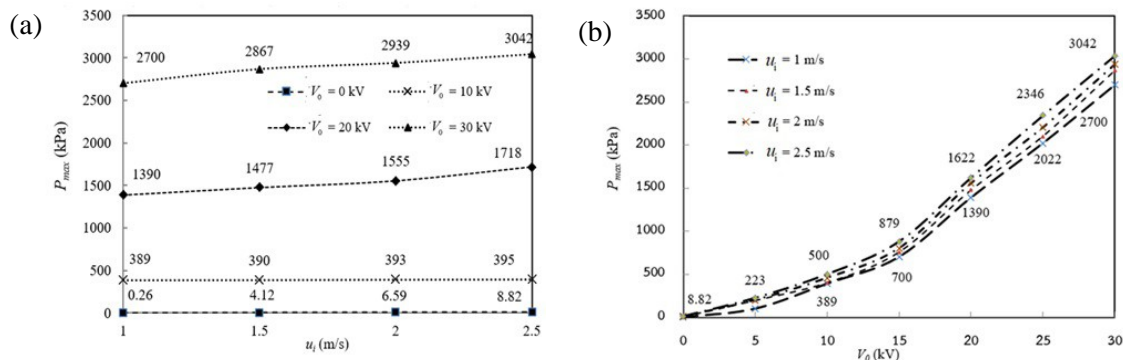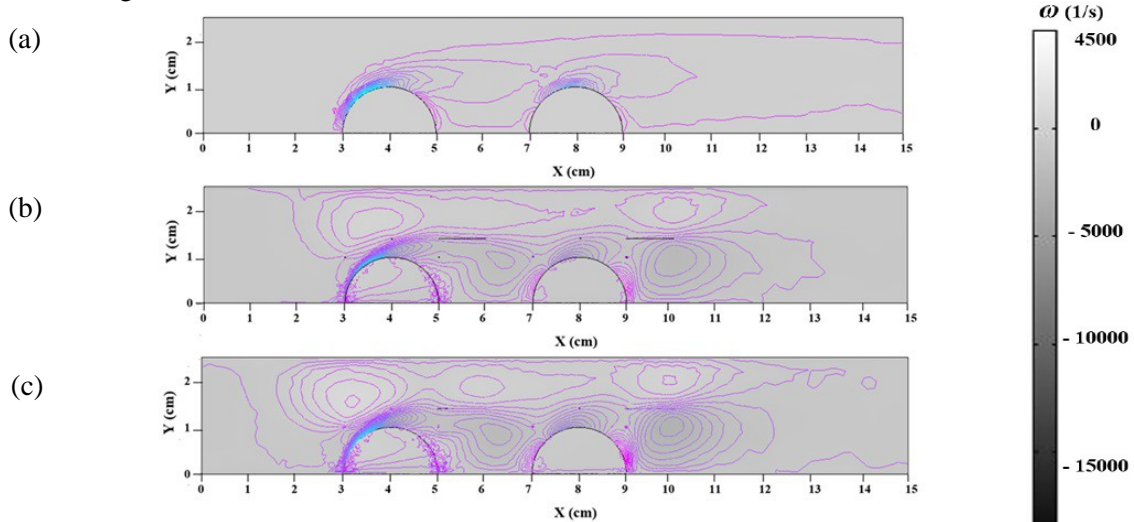

Fig. 16 Maximum pressure in case of (a) inlet velocity in various electrical voltage (b) electrical voltage in various inlet velocity
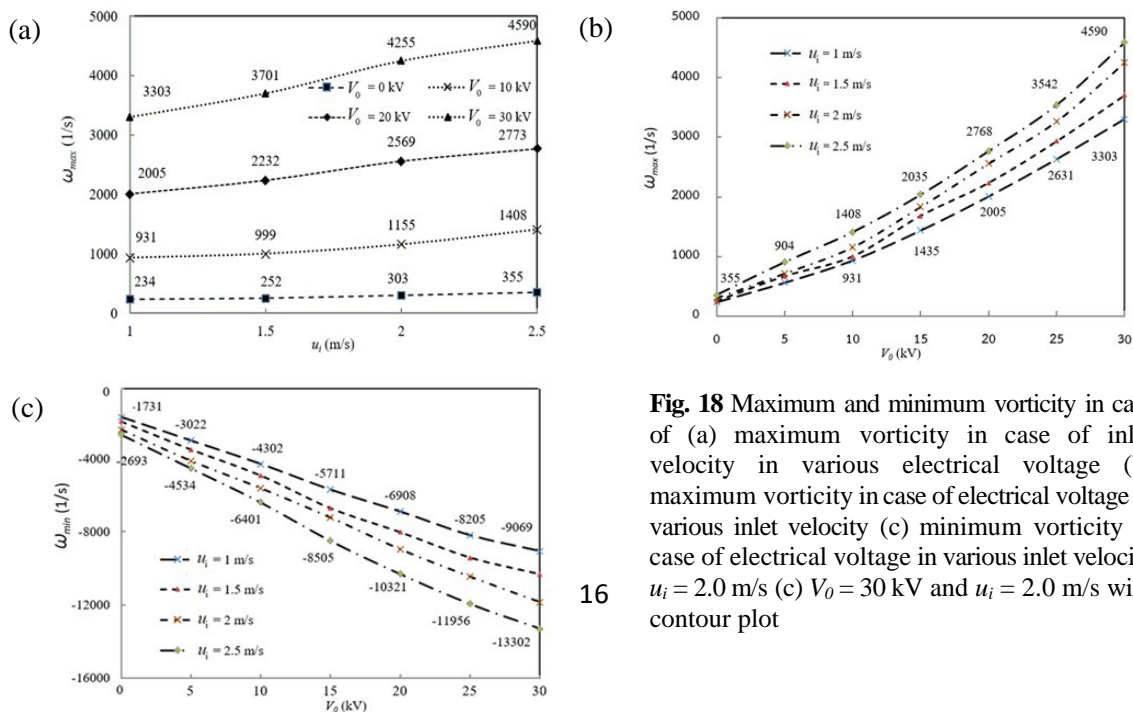
3.5 Effect of vorticity field distribution

The vorticity field within the water channel with and without the electrostatic precipitator process is compared in Fig. 17. The vorticity is a pseudovector field that can describe the trend and direction of particle rotation. Conceptually, vorticity could be determined by marking parts of a continuum in a small neighborhood of the point in question and watching their relative displacements as they move along the flow. In all cases, the contour of vorticity is swirling and turbulent around the porous samples. The vorticity contour with the electrostatic precipitator process (Fig. 17 (b - c)) is more concentrated than without (Fig. 17 (a)). In addition, high inlet velocity and electrical voltage can more disturb the contour of vorticity than low inlet velocity and absent electrical voltage. The vorticity would be twice the mean angular velocity vector of those particles relative to their center of mass, oriented according to the right-hand rule. The value of vorticity in various inlet velocities and electrical voltage is shown in Fig. 18. The maximum vorticity (ω_{max}) is increased with inlet velocity (Fig. 18 (a)) and electrical voltage increasing (Fig. 18 (b)). The graph of maximum vorticity (ω_{max}) is a variable straight line for inlet velocity increasing (u_i), and it is the variable exponential line for the electrical voltage (V_0), $\omega_{max} \propto u_i \propto V_0^2$. But the minimum vorticity (ω_{max}) is decreased with electrical voltage and inlet velocity increasing (Fig. 18 (c)).

Fig. 17 Vorticity field within water channel (a) $V_0 = 0$ kV and $u_i = 1.0$ m/s (b) $V_0 = 20$ kV and $u_i = 2.0$ m/s (c) $V_0 = 30$ kV and $u_i = 2.0$ m/s with contour plot

Fig. 18 Maximum and minimum vorticity in case of (a) maximum vorticity in case of inlet velocity in various electrical voltage (b) maximum vorticity in case of electrical voltage in various inlet velocity (c) minimum vorticity in case of electrical voltage in various inlet velocity $u_i = 2.0$ m/s (c) $V_0 = 30$ kV and $u_i = 2.0$ m/s with contour plot

3.6 Effect of temperature field distribution

The graph of the isothermal surface is explained in terms of the temperature field; all points of the same temperature are connected in the field. The temperature field within the water channel with and without the electrostatic precipitator process is compared in Fig. 19. The heat transfer from water transport through the sample, so the temperature within the porous sample gradually increases. Temperature field due to time-dependent heat sources in a large rectangular grid. With absent electrostatic precipitator process, $u_i = 1.0$ m/s and first stage ($t = 0$ s) (Fig. 19 (a)), uniform initial temperature of water (T_i) is 30 ºC (303 K) and initial temperature of saturated porous samples (T_s) are 10 ºC (283 K). As time progresses ($t = 0.5$ s) (Fig. 19 (b)), heat from water transfers into the sample, so the temperature within the porous sample gradually increases. Within water channel under the k-ε turbulent model, the contour line of temperature in case of high inlet velocity, electrical voltage and time ($u_i = 2.5$ m/s, $V_0 = 30$ kV and $t = 0.6$ s) (Fig. 19 (d)) can more disturb than in case of low inlet velocity, electrical voltage and time ($u_i = 1.0$ m/s, $V_0 = 5$ kV and $t = 0.2$ s) (Fig. 19 (c)). Figure 20 shows the relationship between the interface zone (center of surface temperature) of saturated porous samples and time with various electrical voltage and $u_i = 1.0$ m/s. The first semicircle shape (front porous sample; T_f) and second semicircle shape (back porous sample; T_b) are shown in Fig. 20 (a) and Fig. 20 (b), respectively. The graph of a parabolic function is shown at the interface zone of temperature. As time progresses, the heat is transferred from water to the sample, so the water flow temperature is decreased. In the final process, the temperature of the sample is closest to the airflow temperature. As a result, it is almost the thermal equilibrium. Therefore, the surface temperature of high electrical voltage ($V_0 = 30$ kV) is higher than in the case of absent electrical voltage ($V_0 = 0$ kV), as shown in Fig. 20 (c). In addition, increasing the electrical voltage and inlet velocity speed up the sample's surface temperature to close to the water flow temperature.

4. Heat transfer enhancement on saturated porous samples using electrostatic precipitator process

This section investigates the flow and temperature fields with the improvement of thermal efficiency within saturated porous samples. This feasibility study is based on the concept of the electrostatic precipitator process; the electrical voltage (V_0) and time are varied from 0 to 30 kV and 0 – 1 s. The inlet velocity of water (u_i) is compared with 1 and 2.5 m/s. From the initial time of the k-ε turbulent model ($t = 0$ s), the uniform initial temperature of water (T_i) is 30 ºC (303 K), and the initial temperature of saturated porous samples (T_s) is 10 ºC (283 K). The inlet velocity is fixed at $u_i = 2.0$ m/s, as shown in Fig. 21 and 22. Figure 21 shows the flow field within saturated porous samples in various electrical voltages. The flow can move from the left to right through both saturated porous samples and is concentrated with high electrical voltage. In all cases, swirling flow is circulated clockwise between the front and back porous samples due to the space between samples. In cases of low electrical voltage ($V_0 = 0 – 5$ kV) (Fig. 21 (a - b)), fluid velocity within the front porous sample is similar to fluid velocity within the back porous samples. But fluid velocity within the front porous sample is higher than ($V_0 = 10 – 15$ kV) (Fig. 21 (c - d)). In cases of high electrical voltage ($V_0 = 20 – 30$ kV) (Fig. 21 (e - g)), fluid velocity within the front porous sample is fluid velocity within the back porous sample, as shown in cases of medium electrical voltage higher than fluid velocity within the back porous sample. The fluid velocity of the left side is more than the right side of the front porous medium, and the fluid velocity of the left and right sides of the back porous medium is rather steady.

From the above date, the flow can move from the left to right direction within the samples, and it can induce temperature within both saturated porous samples, as shown in Fig. 22. The temperature field in case of $V_0 = 0 – 30$ kV (Fig. 22 (a - g)) is increased by flow field in Fig. 21 (a - g), respectively. In addition, the inlet velocity of the water channel under the k-ε turbulent model (u_i) is compared with 1 and 2.5 m/s, as shown in Fig. 23. In $t = 0.05$ s, the temperature within the saturated porous sample surface between the first semicircle shape (front porous

sample; T_f) and the second semicircle shape (back porous sample; T_b) is compared in various electrical voltage and initial velocity. In all cases, the value of the temperature of the interface zone (center of surface temperature) in the case of high inlet velocity ($u_{i=}$ 2.5 m/s) is higher than in the case of low inlet velocity ($u_{i=}$ 1.0 m/s).

The temperature value in the first semicircle shape (front porous sample; T_f) is higher than in the case of the second semicircle shape (back porous sample; T_b). In addition, the graph of the value of temperature (T) is a variable straight line for electrical voltage increasing (V_0), $T \propto V_0$.

(a)

(b)

(c)

(d)
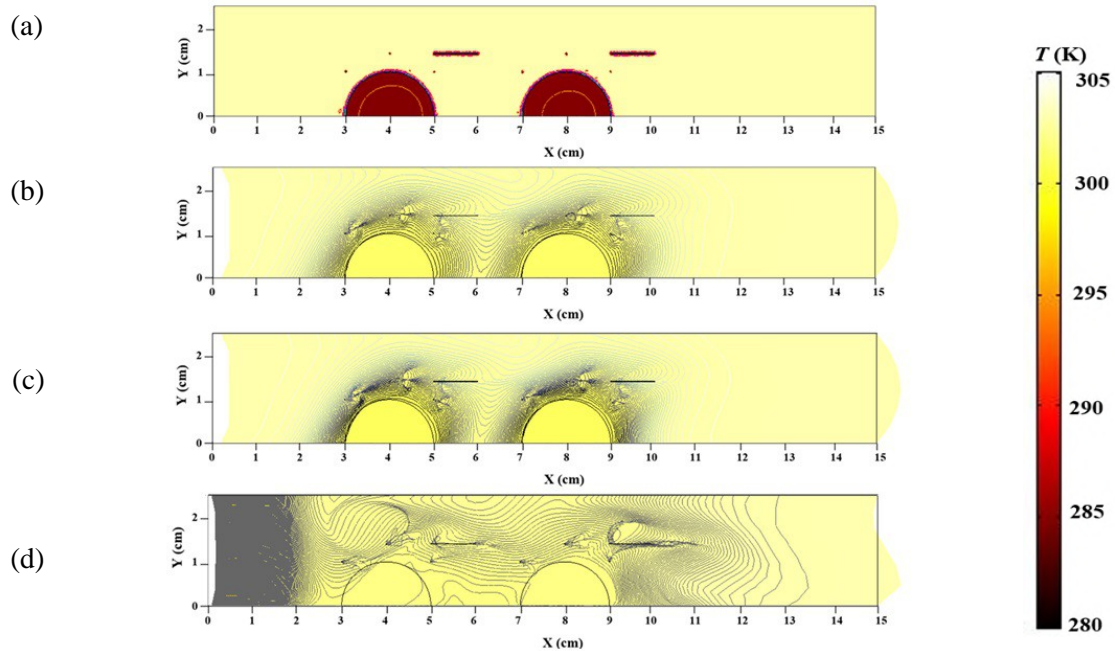
Fig. 19 Temperature field within water channel and with and without electrostatic precipitator process (a) $u_i = 1.0$ m/s, $V_0 = 0$ kV and $t = 0$ s (b) $u_i = 1.0$ m/s, $V_0 = 0$ kV and $t = 0.5$ s (c) $u_i = 1.0$ m/s, $V_0 = 5$ kV and $t = 0.2$ s (d) $u_i = 2.5$ m/s, $V_0 = 30$ kV and $t = 0.6$ s with contour plot and deformed shape

(a)

(b)

(c)
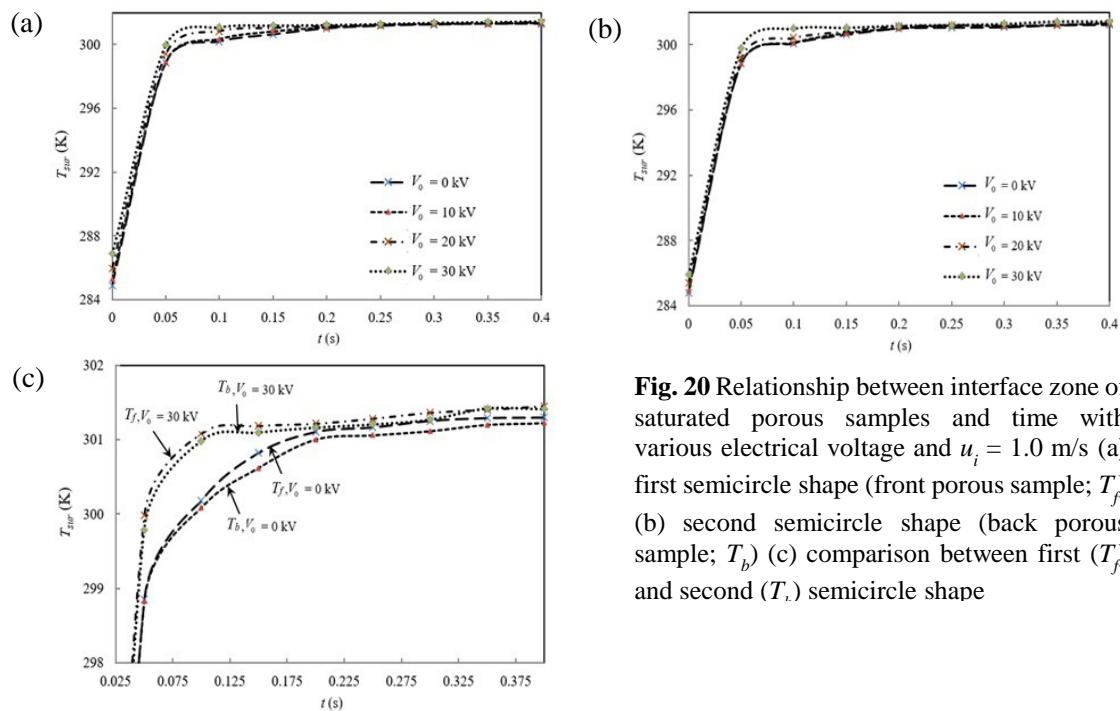
Fig. 20 Relationship between interface zone of saturated porous samples and time with various electrical voltage and $u_i = 1.0$ m/s (a) first semicircle shape (front porous sample; T_f) (b) second semicircle shape (back porous sample; T_b) (c) comparison between first (T_f) and second (T_b) semicircle shape
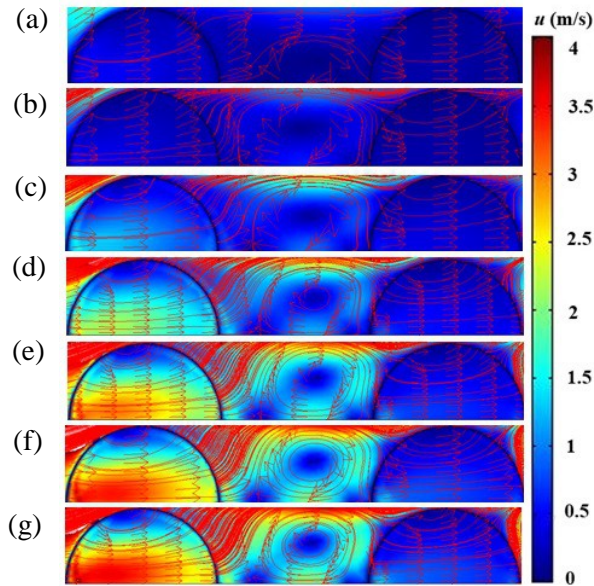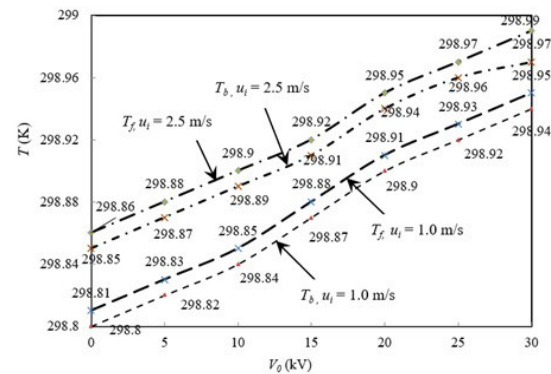
Fig. 21 Flow field within saturated porous sample with $u_i = 2.0$ m/s (a) $V_0 = 0$ kV (b) $V_0 = 5$ kV (c) $V_0 = 10$ kV (d) $V_0 = 15$ kV (e) $V_0 = 20$ kV (f) $V_0 = 25$ kV (g) $V_0 = 30$ kV with streamline and arrow plot
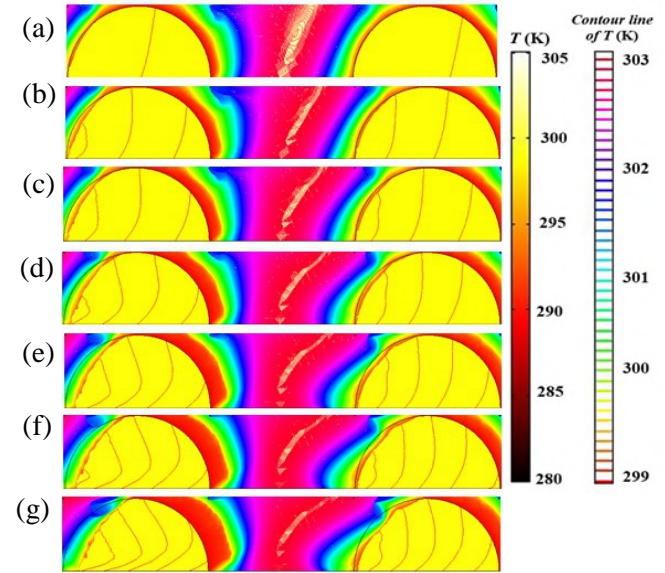
Fig. 22 Temperature field within saturated porous sample with $u_i = 2.0$ m/s and $t = 0.05$ s (a) $V_0 = 0$ kV (b) $V_0 = 5$ kV (c) $V_0 = 10$ kV (d) $V_0 = 15$ kV (e) $V_0 = 20$ kV (f) $V_0 = 25$ kV (g) $V_0 = 30$ kV with contour plot and deformed shape
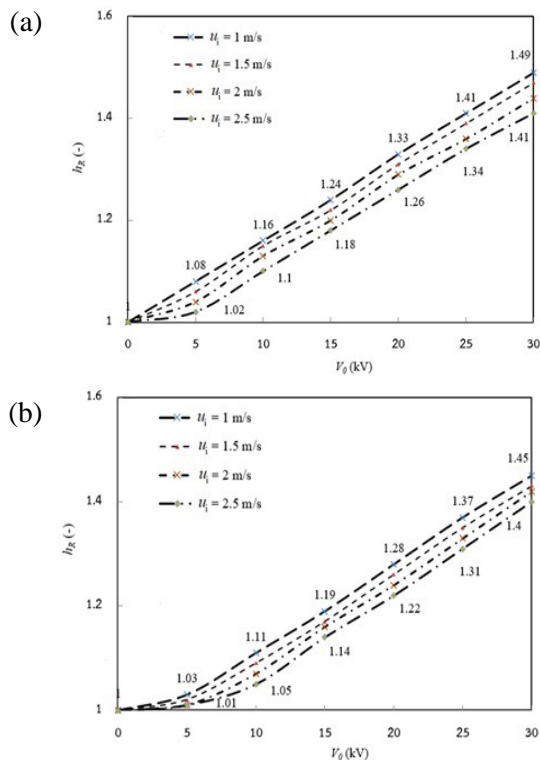
Figure 24 compares the local heat transfer coefficient ratio (h_R) with $t = 0.1$ s between the electrical voltage in various inlet velocities within the saturated porous sample. In mechanics and thermodynamics, the heat transfer coefficient is the proportionality constant between the heat flux and the thermodynamic driving force for the flow of heat. The local heat transfer coefficient (h_L) at a particular point on the heat transfer surface is equal to the local heat flux, at the same point, per the local temperature drop. The first semicircle shape (front porous sample; T_f) and second semicircle shape (back porous sample; T_b) are investigated in Fig. 24 (a) and 24 (b), respectively. The local heat transfer coefficient ratio (T) is referred to as the local heat transfer coefficient when using the electrostatic precipitator process (*EP*) per local heat transfer coefficient in the absent electrostatic precipitator process (no *EP*), i.e., $h_{L,EP} / h_{L,noEP}$. The heat transfer within the samples is enhanced by the fluid flow in the water channel, so the local heat transfer coefficient within the samples is induced by fluid velocity in the water channel.

Fig. 23 Temperature comparisons within saturated porous sample surface between the first semicircle shape (front porous sample; T_f) and the second semicircle shape (back porous sample; T_b) in various electrical voltage and initial velocity ($u_i = 1.0$ m/s and 2.5 m/s) and $t = 0.05$ s

The graph of the local heat transfer coefficient ratio (h_R) (Fig. 24) shows a similar trend to the fluid velocity ratio (Fig. 14 (b)). The local heat transfer coefficient ratio decreases with inlet velocity increasing and increases with the electrical voltage increases. The local heat transfer coefficient ratio graphs are variable exponential lines for the electrical voltage (V_0), $h_L \propto V_0^2$; this is because the fluid velocity within the front porous sample is higher than the back porous sample. Consequently, the first semicircle

shape's local heat transfer coefficient ratio (front porous sample; T_f) is higher than the second semicircle shape (back porous sample; T_b).

(a)

(b)

Fig. 24 Comparison on local heat transfer coefficient ratio with $t = 0.1$ s between electrical voltage in various inlet velocity within saturated porous sample (a) first semicircle shape (front porous sample; T_f) (b) and the back semicircle shape (back porous sample; T_b)

5. Conclusion

The heat transfer enhancement on saturated porous samples is numerically investigated using the electrostatic precipitator process. The water channel is solved in this study using the k-ε turbulent model. In the first part, the simulated result of flow visualization is validated against the experimental result. It can be seen that a similar trend of the airflow distribution has appeared in both cases.

For the second part, the disturbance of electric field distribution can create a more concentrated electrical potential, resulting in the turbulent area appearing. The flow field moves from the left to the right direction, avoiding both saturated porous samples. The electric force is induced from the electric field resulting in the circulating flow that can induce the fluid flow within the water

channel under the k-ε turbulence model. The pressure field in the case of the electrostatic precipitator process is more concentrated than in the absent case. In addition, higher inlet velocity and high electrical voltage can induce greater pressure than in other cases. The contour of vorticity is swirling and turbulent around the porous samples. The contour line of temperature in case of high inlet velocity, electrical voltage, and time can be more disturbing than in the case of low inlet velocity, electrical voltage, and time.

The flow and temperature fields were investigated with heat transfer enhancement within saturated porous samples for the last part. The flow can move from the left to right direction within both saturated porous samples and induce temperature within both. The value of the temperature in the case of the first semicircle shape is higher than in the case of the second semicircle shape. The heat transfer within samples is enhanced from fluid flow in the water channel, so the local heat transfer coefficient within samples is induced from fluid velocity in the water channel.

References

[1] W. Yuansong, T.V.H. Renze, R.B. Arjen, H.E. Dock, F. Yaobo, Minimization of excess sludge production for biological wastewater treatment. Water Research 37(18) (2003) 4453 - 4467.

[2] W. Britt-Marie, Bojin P, The influence of key chemical constituents in activated sludge on surface and flocculating properties. Water Research 37(9) (2003) 2127 - 2139.

[3] L. Yu, Chemically reduced excess sludge production in the activated sludge process. Chemosphere 50(1) (2003) 1 - 7.

[4] L. Bing, L. Tong, Biodegradation and Adsorption of Antibiotics in the Activated Sludge Process. Environmental Science and Technology 44 (2010) 3468 - 3473.

[5]   F. Çeçen1, G. Gül, Biodegradation of five pharmaceuticals: estimation by predictive models and comparison with activated sludge data. International Journal of Environmental Science and Technology 18 (2020)327 - 340.

[6]   H. Nouri, N. Zouzou, E. Moreau, L. Dascalescu, Y. Zebboudj, Effect of relative humidity on current-voltage characteristics of an electrostatic precipitator. Journal of Electrostatics 70(1) (2012) 20 - 24.

[7]   Y. Zhenda, Z. Chengheng, L. Shaojun, G. Yishan, L. Chengsi, W. Yi, H. Daqing, G. Xiang, A combined wet electrostatic precipitator for efficiently eliminating fine particle penetration. Fuel Processing Technology 180 (2018) 122 - 129.

[8]   M. Anvari, N, Shadjou,Dendritic fibrous nanosilica functionalized by dithiocarbamate as a highly efficient adsorbent for the removal of malachite green from waste water based on electrostatic interaction. International Journal of Environmental Science and Technology 18 (2021)1089 - 1096.

[9]   M. Jerzy, K. Marek, D. Jaroslaw, D. Miroslaw, P. Janusz, O. Toshikazu, K. Seiji, K. Toshiyuk, Measurements of the velocity field of the flue gas flow in an electrostatic precipitator model using PIV method. Journal of Electrostatics 51-52 (2001) 272-277.

[10] Z. Lin, A. Kazimierz, Numerical simulation of the electrohydrodynamic flow in a single wire-plate electrostatic precipitator. IEEE Transactions on Industry Applications 44(3) (2008) 683 – 691.

[11] N. Farnoosh, K. Adamiak, G.S.P. Castle, Three dimensional analysis of electrohydrodynamic flow in a spiked electrode-plate electrostatic precipitator. Journal of Electrostatics 69 (2011) 419 - 428.

[12] V. Audrey, G. Yves, G. Evlyne, B. Alain, R. Serge, G. Maguelone, G. Jacques, Separation of particles from syngas at high-temperatures with an electrostatic precipitator. Separation and Purification Technology 92(18) (2012) 181 - 190.

[13] D. Hao, L. Yong, N. TszWai, H. Guocheng, X. Shangchao, X. Xin, Y. Shijian, K. Po, The simultaneous centralized control of elementalmercury emission and deep desulfurization from the flue gas using magnetic Mn–Fe spinel as a Co-benefit of the wet electrostatic precipitator. Fuel Processing Technology 142 (2016) 345 - 351.

[14] S.S. Taghayi, N. Fadaki, H.M. Amanifard, Deylami, F. Dolati, Numerical analysis of the EHD driven flow with heat transfer in a smooth channel using multiple collectors. Heat and Mass Transfer (53) (2017) 2445 - 2460.

[15] H.M. Deylami, Effects of EHD on the flow and heat transfer characteristics in a rectangular corrugated channel. Heat and Mass Transfer (55) (2019) 3711 - 3720.

[16] P. Milad, M. Amirhosein, S. Constantinos, Evaluation of a high flow rate electrostatic precipitator (ESP) as a particulate matter (PM) collector for toxicity studies. Science of The Total Environment (15) (2020) 140060.

[17] C. Jingcai, D. Yong, W. Zhiqiang, W. Peng, C. Peng, M. Chunyuan, Removal of sulfuric acid aerosol in a wet electrostatic precipitator with single terylene or polypropylene collection electrodes. Journal of Aerosol Science 42(8) (2011) 44 - 554.

[18] D. Liton, V. Chandra, A wet electrostatic precipitator (WESP) for soft nanoparticle collection. Aerosol Science and Technology 46(7) (2012) 750 - 759.

[19] C. Beelee, S.W. Anthony, C.T. Norman, A.N. Debbie, A.H. Britt, Collection of liquid phase particles by microfabricated electrostatic precipitator. Journal of Microelectromechanical Systems 22(5) (2013) 1010 – 1019.

[20] T. Islam, N. Parveen, F.-Al-Asad, Hydromagnetic Natural Convection Heat Transfer of Copper-Water Nanofluid within a Right-Angled Triangular Cavity. International Journal of Thermofluid Science and Technology 7 (3) (2020) Paper No. 07030.

[21] T. Yamamoto, H.R. Velkoff, Electrohydro-dynamics in an electrostatic precipitator. Journal of Fluid Mechanics 108 (1981) 1-18.

[22] S. Saneewong Na Ayuttaya, A review of electrohydrodynamics application (Based on the mechanism characteristic). Chulachomklao Royal Military Academy Journal 15 (2017) 37 - 59.

[23] H. Sergio, J. Javier, Scaling of the velocity fluctuations in turbulent channels up to Re_T =2003. Physics of Fluids 18 (2006) 011702 - 4.

[24] A.A. Afify, MHD free convective flow and mass transfer over a stretching sheet with chemical reaction. Heat and Mass Transfer 40 (2004) 495 - 500.

[25] F. Wolfram, W. Tino, T. Holger, S. Hans-Peter, Smoke surfaces: An interactive flow visualization technique inspired by real-world flow experiments. IEEE Transactions on Visualization and Computer Graphics 14(6) (2008) 1396 – 1403.

[26] L.O. William, G.T. Timothy, Verification and validation in computational fluid dynamics. Progress in Aerospace Sciences 38(3) (2002) 209 - 272.

[27] P. Eiamsa-ard, N. Piriyarungroj, C. Thianpong, S. Eiamsa-ard, A case study on thermal performance assessment of a heat exchanger tube equipped with regularly-spaced twisted tapes as swirl generators. Case Studies in Thermal Engineering 3 (2014) 86 - 102.

[28] F.M. White, Fluid Mechanics. 8th ed. New York: McGraw-Hill Book Company (2020).

[29] S. Saneewong Na Ayuttaya, C. Chaktranond, P. Rattanadecho, Numerical analysis of electric force influence on heat transfer in a channel flow (Theory based on saturated porous medium approach). International Journal of Heat and Mass Transfer 64 (2013) 361 - 374.

[30] S. Saneewong Na Ayuttaya, P. Rattanadecho, Influence of electrode arrangements on electro-hydrodynamics and transport phenomenon within water and porous samples connected to rectangular duct. International Journal of Thermal Sciences 130C (2018) 367 - 385.

[31] U. Osman, Estimation of the porosity of clay soils using seismic P- and S-wave velocities. Journal of Applied Geophysics 170 (2019) 103832.

[32] S. Saneewong Na Ayuttaya, C. Chaktranond, P. Rattanadecho, T. Kreewatcharin, Effect of Ground Arrangements on Swirling Flow in a Rectangular Duct Subjected to Electrohy-drodynamic Effects. Journal of Fluids Engineering-Transactions of the ASME 134 (2012) 051211 - 9.

[33] D.J. Griffiths, Introduction to electrohydro-dynamics, Prentice Hall International, Inc. New Jersey (1999) 54.

[34] W. Klinbun, P. Rattanadecho, Numerical model of microwave driven convection in multilayer porous packed bed using a rectangular waveguide. ASME Journal of Heat Transfer 134 (2012) 0426051 - 10.

[35] X. Ruoyu, Z. Hingjie, Y. Jie, Electric-field intrabody communication channel modeling with finite-element method. IEEE Transactions on Biomedical Engineering 58(3) (2017) 705 - 712.

[36] S. Hadi, M. Hamid, H. Saeed, F.M. Reza, Electrospinning of polyacrylonitrile nanofibers and simulation of electric field via finite element method. Nanomedicine Research Journal 2(2) (2017) 87 - 92.

[37] S. Saneewong Na Ayuttaya, Numerical analysis of jet air flow impact inclined flat plate under electrohydrodynamics force in a porous medium. International Journal of Numerical Methods for Heat and Fluid Flow 31(7) (2021) 2373 - 2404.